Nanoscale

ROYAL SOCIETY OF CHEMISTRY

PAPER

View Article Online
View Journal | View Issue

Cite this: *Nanoscale*, 2026, **18**, 4440

# Amplified spontaneous emission dependence on temperature-induced crystalline phase transition in a solution processed $MAPbBr_3$ thin film

Maria Luisa De Giorgi, *[a] Titti Lippolis,[a] Nur Fadilah Jamaludin,[b] Cesare Soci, [c] Annalisa Bruno [b] and Marco Anni [a]

Received 27th October 2025,
Accepted 18th December 2025

DOI: 10.1039/d5nr04524j

rsc.li/nanoscale

Hybrid metal–halide perovskites are attracting huge research interest for possible applications in opto-electronic and photonic devices. In particular, the demonstration of optical gain and amplified spontaneous emission (ASE) at room temperature stimulates their development as active materials in light amplifiers and lasers. However, understanding of the basic photophysics of the processes affecting the ASE properties to date is still limited. In this work, we report a systematic investigation of the temperature dependence of the ASE and the photoluminescence (PL) of an $MAPbBr_3$ thin film in the 20–300 K range. We confirm that the ASE threshold is strongly temperature dependent, due to the thermal activation of non-radiative processes. In addition, the ASE temperature dependence shows clear discontinuities at around 90 K and 190 K, related to the orthorhombic–tetragonal and tetragonal–cubic phase transitions, respectively. The film spontaneous emission under nanosecond and continuous wave pumping shows the interplay of emission of Free Excitons (FEs), Bound Excitons (BEs), and trap states, with relative contributions depending on the temperature and the excitation regime. Our findings result in a detailed description of the energy states generating the ASE and the ASE properties of the different crystalline phases.

## Introduction

In the last decade, hybrid metal lead halide perovskites, such as $APbX_3$ (where A = organic cation and X = inorganic halide anion – Cl, Br, or I or mixed Cl/Br and Br/I systems) have attracted attention as alternative, low-cost and efficient photovoltaic materials[1,2] due to their large absorption coefficients, excellent charge mobilities, and high diffusion lengths.[3–13]

In addition, these materials exhibit good light emission properties, such as high emission quantum yield and optical gain, that allow them to be employed as active media for light-emitting diodes (LEDs),[14–21] light-emitting transistors,[22] and lasers.[20–23]

Among the many lead halides perovskites showing optical gain,[23] efficient amplified spontaneous emission (ASE) at room temperature has been demonstrated in a bromine-based methylammonium lead hybrid perovskite ($MAPbBr_3$), allowing its use as an active material in optically pumped green perovskite lasers.[24–26] In particular, ASE has been observed under pulsed optical pumping in the femtosecond regime in $MAPbBr_3$ single-[27] and micro-[28] crystals, as well as in thin films[29–32] with thresholds ranging from a few up to about a hundred μJ $cm^{-2}$, and in the nanosecond regime in polycrystalline films[26,33–36] with thresholds between 35 and 300 μJ $cm^{-2}$.

These results, that suggest possible applications of $MAPbBr_3$ in efficient light amplifiers and lasers in the green, stimulate basic physics experiments to understand the processes affecting the $MAPbBr_3$ optical properties.

In this frame, optical and structural measurements below room temperature evidenced the presence of several features affecting the photoluminescence spectra and the relaxation dynamics of thin films, single crystals and nanocrystals of lead halide perovskites in general[37–42] and of $MAPbBr_3$ in particular,[43–48] like the presence of light emitting traps, temperature-induced crystalline phase transitions and thermally induced emission quenching.

However, to date, investigation of the dependence of the optical properties on temperature has been mostly focused on absorption and photoluminescence,[43,45–47] while the temperature dependence of the ASE properties has rarely been investigated, with only a few experiments on $MAPbI_3$ thin films,[49,50] bulk polycrystalline $CsPbBr_3$[51] and nanocrystal thin films.[52] In contrast, the temperature dependence of the ASE properties of $MAPbBr_3$ is to date fully unexplored.

---

[a] *Dipartimento di Matematica e Fisica "Ennio De Giorgi", Università of Salento, 73100 Lecce, Italy. E-mail: marialuisa.degiorgi@unisalento.it*
[b] *Energy Research Institute @ NTU (ERI@N), Nanyang Technological University, 637553, Singapore*
[c] *Division of Physics and Applied Physics, School of Physical and Mathematical Sciences, Nanyang Technological University, 637371, Singapore*

In this work, we aim to fill this gap by temperature-dependent ASE and photoluminescence measurements on a solution-processed $MAPbBr_3$ thin film in the 20–300 K range.

We demonstrate that under pulsed nanosecond pumping, the film shows ASE in the whole temperature range, with a strongly temperature-dependent ASE threshold ascribed to the thermal activation of non-radiative processes. The ASE temperature dependence shows clear discontinuities at around 90 K and 190 K, related to the orthorhombic–tetragonal and tetragonal–cubic phase transitions, respectively, leading to different activation energies and coupling rates of the non-radiative process.

We also show that the film spontaneous emission under nanosecond and continuous wave pumping shows the interplay of emission of Free Excitons (FEs), Bound Excitons (BEs), and trap states (visible only below 100 K), with relative contributions depending not only on the temperature, but also on the excitation regime.

Finally, we show that the ASE comes from BEs in the whole temperature range and that, among the three phases, the orthorhombic one shows the intrinsically best ASE properties, with the lowest ASE values and the smallest temperature dependence.

Our results provide valuable insights into the fundamental optical properties of $MAPbBr_3$ thin films, evidencing the fundamental role of the crystalline phase in ASE properties and that of the trap related emission in PL properties, which can be useful to guide further improvements of the emission properties of hybrid lead halide perovskites for applications in photonics and optoelectronic devices.

Despite the rapid progress in research on the photoluminescence (PL) properties of metal halide perovskite materials, a comprehensive understanding of the correlation between the structural phases of lead-halide perovskite films and their amplified spontaneous emission (ASE) characteristics is still missing. Addressing this knowledge gap constitutes a central innovative contribution of our study.

# Experimental

### Sample fabrication

The $MAPbBr_3$ film was synthesized from a solution prepared by dissolving MABr and $PbBr_2$ in a DMF : DMSO cosolvent (25% DMSO) at a ratio of 1.05 : 1. It was deposited by spin-coating 40 μL of the perovskite solution onto a quartz substrate at 5000 rpm for 30 s, followed by toluene dripping 5 s later. Then it was dried under vacuum for 30 min. Beforehand, the substrate was sequentially cleaned in a decon soap with deionized water and isopropanol for 15 min each, then blow dried with $N_2$ and ozone-treated for 30 min.[34]

The obtained film had a thickness of about 120 nm.

### Absorption, photoluminescence and amplified spontaneous emission

The ASE properties were explored by pumping the film with an LBT MNL100 nitrogen laser at 337 nm, delivering 3 ns pulses at a repetition rate of 10 Hz.

In order to compare the ASE properties with the characteristic photoluminescence, PL experiments were performed at a low energy density by exciting the samples with a cw solid state laser at a wavelength of 405 nm, with a power of 1 mW.

All the measurements were performed by collecting the signal in the waveguide configuration from the edge of the film irradiated with the beam focused in a rectangular stripe (4 mm × 80 μm). The emission was acquired using an optical fiber coupled to a spectrometer (ACTON SpectraPro-750) equipped with a Peltier cooled-CCD (Andor). The spectral resolution was about 0.5 nm.

The measurements were performed under vacuum (at a pressure of about $10^{-2}$ mbar) at temperatures from 300 K down to 20 K in steps of 20 K using a closed cycle He cryostat.

The UV–vis absorption spectrum was acquired using a spectrophotometer (PerkinElmer Inc., Waltham, MA, USA, model UV–vis Lambda 900). The absorption compared with a typical photoluminescence spectrum is shown in Fig. S1 of the SI.

# Results and discussion

### Amplified spontaneous emission

The ASE properties of the film were investigated in the ns-regime by cooling the sample from room temperature (RT, 300 K) down to $T$ = 20 K.

As a first step, we acquired the PL spectra as a function of the excitation density at RT (see Fig. 1a).

At a low excitation density, the PL spectrum shows two spontaneous emission (SE) bands at about 530 nm and 544 nm, with Full Width at Half Maximum (FWHM) of about 13 nm and 35 nm, respectively (as an example, the two bands are evidenced through the deconvolution of the spectrum acquired at 0.24 mJ $cm^{-2}$ and reported in the SI in Fig. S2a). The narrow lineshape and the spectral position of the peak at

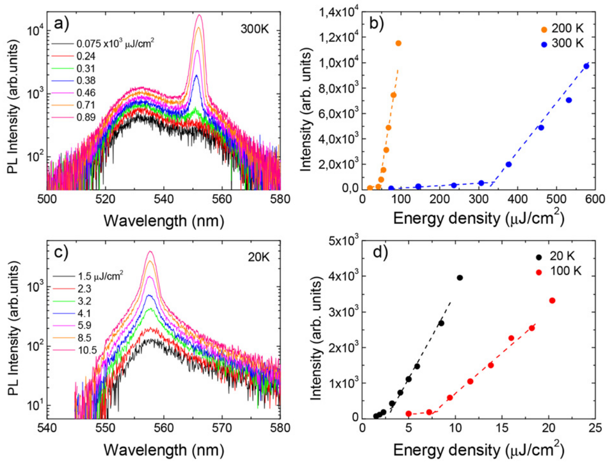

**Fig. 1** PL spectra as a function of the excitation density at (a) 300 K and (c) 20 K showing the gradual appearance of the ASE peak with increasing excitation density. Excitation density dependence of the emission intensity at ASE peak wavelengths of (b) 300 K and 200 K and (d) 100 K and 20 K.

530 nm with respect to the exciton absorption peak (see Fig. S1) allow this peak to be ascribed to Free Exciton (FE) emission, while the broad peak at 544 nm can be ascribed to Bound Excitons (BEs), as also suggested in previous papers.[53–55]

As the excitation density increases, the PL intensity progressively increases, accompanied by the appearance, at about 300 µJ cm$^{-2}$, of a narrow band centered at about 552 nm, typical of ASE, that gradually dominates the emission as the excitation density further increases.

The excitation density dependence of the emission intensity at the ASE peak wavelength (see Fig. 1b) shows an evident slope increase corresponding to the appearance of the ASE peak in the spectrum. At 300 K, the ASE threshold, defined as the lowest excitation density that allows observation of the ASE induced line-shape variation (also called visual threshold[56]), is estimated to be 307 µJ cm$^{-2}$.

The excitation density dependence of the PL spectra was also investigated at lower temperatures (200 K, 100 K, and 20 K). The obtained results are qualitatively similar to those obtained at 300 K, with the presence of the ASE peak at high excitation densities (the results at 20 K are presented in Fig. 1c, as an example). Nevertheless, with the decrease of the temperature, the ASE threshold value strongly decreases (down to 43 µJ cm$^{-2}$, 9.4 µJ cm$^{-2}$ and 2.3 µJ cm$^{-2}$, for $T$ = 200 K, 100 K, and 20 K, respectively) and the ASE intensity increases (see Fig. 1b and d). Furthermore, by decreasing the temperature, the ASE process gradually becomes more efficient, as can be inferred from the slopes of the *I versus* energy density curves estimated from the linear fits of the plots (29.7 ± 2.2, 220 ± 15, 236 ± 11 and 498 ± 24 (µJ cm$^{-2}$)$^{-1}$ for $T$ = 300 K, 200 K, 100 K, and 20 K, respectively).

To have a more detailed understanding of the ASE temperature dependence, we also acquired, over the whole temperature range, the emission spectra at an excitation density of 900 µJ cm$^{-2}$, that is about 3 times the highest determined threshold (at RT).

The two-dimensional (2D) map of the temperature dependence of the spectra above the ASE threshold (see Fig. 2a) evidences that, as the temperature decreases, the spontaneous emission contribution to the spectra progressively becomes less evident, which is consistent with the ASE threshold reduction and ASE intensity increase.

A progressive shift of the ASE peak can also be observed (see Fig. 2b), with temperature-dependent behavior. In particular, the ASE peak wavelength is initially almost constant between 300 K and 200 K, then it progressively red-shifts from 180 K down to 100 K, suddenly blue-shifts between 100 K and 80 K, and then strongly red-shifts between 80 K and 20 K.

This behavior highlights the presence of three different emission regimes, with transitions at around 190 K and 90 K.

This conclusion is also clearly confirmed by the ASE threshold temperature dependence (see Fig. 2b), showing a progressive exponential decrease as the temperature decreases, but with a clearly discontinuous slope, showing abrupt changes at about 190 K and 90 K.

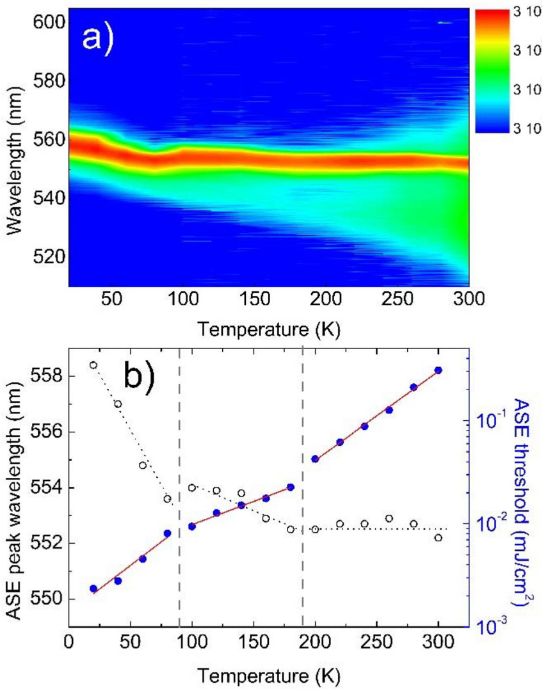

**Fig. 2** (a) 2D map of the emission spectra above the ASE threshold as a function of the temperature. (b) Temperature dependence of the ASE peak wavelength and the ASE threshold.

## Photoluminescence

To rationalize the origin of the observed ASE temperature dependence, we also performed PL measurements under cw-pumping from 300 K down to 20 K. The spectra are shown in Fig. 3a.

Starting from a qualitative comparison, the cw-PL lineshape is very similar to that of the ns-spontaneous emissions (below the threshold) at both 300 K and 200 K (see Fig. S3), while it shows a higher relative contribution to the emission at a high wavelength of 100 K, and is very different at 20 K.

In the range from RT to 120 K, the cw-PL spectra are well fitted by two Gaussian peaks (in the following HE and LE, for the peak at high and low energies, respectively), with a peak position and linewidth comparable to the ones observed for FE and BE emissions under nanosecond pumping below the threshold, suggesting that the emission comes from the same states (see Fig. 3b for the peak position comparison and Fig. S2b for the cw-PL spectrum fit at 300 K).

The relative contribution of these two peaks to the total cw-PL is basically constant between RT and 120 K (see Fig. S4). In contrast, the clear line-shape variation observed below 100 K is due to the appearance of a third peak (named LT1, as only visible at low temperature) between 100 K and 80 K and a fourth peak (LT2) between 60 K and 20 K (see Fig. 3b and Fig. S2d), both at wavelengths higher than the LE peak.

The relative contribution of these two further emission peaks to the total PL intensity continuously increases as the temperature decreases, up to about 70% at 20 K (see Fig. S4),

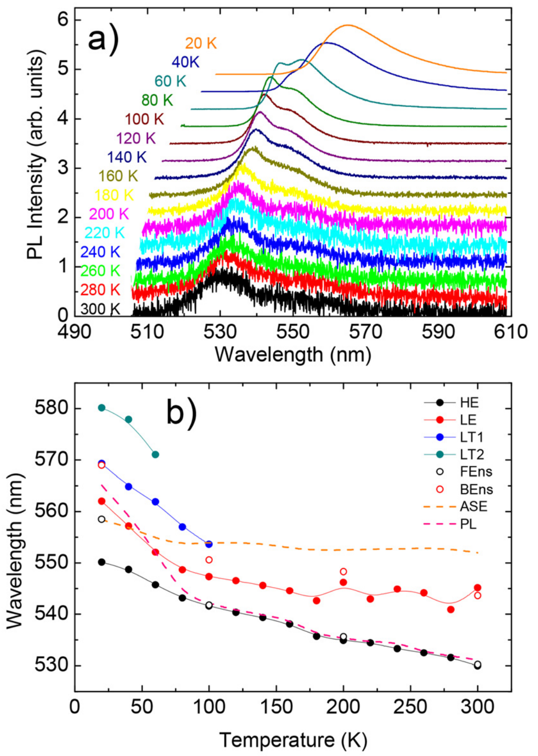

**Fig. 3** (a) PL spectra as a function of the temperature under continuous wave pumping. The spectra are normalized to 1 and vertically translated for clarity. The progressive shift and lineshape variation are clearly visible. (b) Temperature dependence of the peak wavelength of all the peaks contributing to the cw-PL spectra. The empty circles correspond to FE (black) and BE (red) emissions under the nanosecond regime below the threshold. The dashed lines represent the peak wavelength of the ASE band (dark yellow) and the total cw-PL spectra (magenta).

with a corresponding decrease of the LE relative contribution and an almost complete disappearance of the HE peak.

Looking at the peak wavelength temperature dependence (see Fig. 3b), we observe, in the whole temperature range, a progressive red-shift when the temperature decreases and it is very interesting to observe that, as found for the ASE peak wavelength and threshold, the cw-PL peak shift also shows a temperature-dependent behavior.

In particular, the HE emission initially shows a weak red-shift, with a first slope increase between 200 K and 180 K, and a second one between 100 K and 80 K. The LE band instead does not show any evident shift down to about 200 K, then there is a weak shift down to 100 K and a stronger one at lower temperatures, very similar to the red-shift shown by the LT1 and LT2 peaks. Thus, both the ASE and the cw-PL temperature dependence demonstrate that three different emission regimes are present, with transition temperatures at about 190 K and 90 K, in qualitative agreement with previous results in the literature. The investigation of the temperature dependence of the crystalline structure, performed by XRD measurements as a function of the temperature,[57–59] allowed demonstration of the presence of crystalline phase transitions of $MAPbBr_3$ below room temperature.

In particular, $MAPbBr_3$, both in single crystals and in thin films, is characterized by cubic crystalline phase at room temperature and shows phase transitions from the cubic to tetragonal phase at around 230 K, from the tetragonal to orthorhombic phase at around 150 K,[57,58] and from the orthorhombic I to orthorhombic II phase at around 80 K.

In addition, several experiments on the $MAPbBr_3$ PL temperature dependence evidenced a variation of the lineshape and linewidth and intensity temperature dependence at temperatures close to the phase transitions, allowing the PL variations to be related to the crystalline phase change.[43,45–47,57,60]

In $MAPbBr_3$, the continuous change of lattice parameters[61] in the high temperature cubic-tetragonal phase transition typically leads to small effects on the PL spectra,[46,48,60,62–66] while the large entropy and discontinuity in the dielectric constant in the low-temperature orthorhombic–tetragonal transition is accompanied by a sudden variation of the PL spectra. These features are very similar to what we observe, with a small variation of the ASE and PL spectra at around 190 K and a clear PL lineshape variation at around 90 K.

A further structural transition, from orthorhombic I to orthorhombic II, observed by Wang *et al.*[59] at around 80 K could explain the onset of the LT2 peak below 60 K.

We observe anyway that the phase transition temperatures cited above are about 40–50 K higher than the transition temperatures observed in our experiment. Having ruled out the possibility that the actual temperature of the sample is higher due to local heating in the irradiated region under our experimental conditions (both under nanosecond and continuous-wave excitations, see the SI for further details), by considering the properties of the $MAPbBr_3$ film and the excitation energy densities used in our experiment, as discussed in our previous work,[34] the observed difference can be explained by taking into account that in the cited papers, the experiments are performed by heating the sample starting from a low temperature, while in our experiment, we cool the sample starting from room temperature. As the phase transition is a gradual process, there is not an instantaneous and total change of the phase at the transition temperature, but the initial phase is still present beyond the phase transition temperature, and the spectral effects of the phase transition become evident only when the phase transition is almost complete.[48] For this reason, in a cooling-cycle, the transition temperatures appear lower than in a heating cycle, leading to the temperature hysteresis behavior already experimentally observed in $MAPbI_{3-x}Cl_x$ films,[67] and computationally predicted in a pure halide perovskite $MAPbI_3$.[68]

## Energy level diagram

In order to attribute the various emission peaks, we start by observing that the peak wavelength values and the temperature-induced shift of the HE peak under continuous wave excitation are very similar to the ones expected for $MAPbBr_3$ excitons (see Fig. S5), allowing confirmation of the attribution of this peak to FE emission of the dominating phase over the whole temperature range.[48] Moreover, the lack of strong lineshape variation of the LE peak and the smooth temperature dependence of the peak wavelength support ascribing this peak to BE emission throughout the temperature range.

Concerning the LT1 and LT2 peaks, only visible below the tetragonal–orthorhombic phase transition temperature, we can exclude that these peaks are due to a residual emission from tetragonal domains, because the value of their red-shift with respect to the FE emission (about 33 and 100 meV for LT1 and LT2, respectively) is clearly higher than the energy difference between the FE emission of the tetragonal and orthorhombic phases (about 20 meV (ref. 48)).

Analogous low energy peaks have been previously observed in both $MAPbBr_3$ single crystals and thin films, ascribed to emission from the traps induced by the coexistence of ordered and disordered orthorhombic domains at low temperature.[57,60,62,65,66] Furthermore, similar features are also observed in other MA-lead halide perovskites and assigned to defect states in the crystals due to the coexistence of tetragonal and orthorhombic phases.[69–72]

The previous attribution of the peaks visible in the cw-PL spectra allows us to discuss the origin of the sample PL in the two excitation regimes.

Starting from high temperatures, the cw and nanosecond PL spectra are very similar both at 300 K and at 200 K, allowing us to conclude that in both regimes, the sample's PL is mainly due to BE emission (giving rise to about 80% of the total intensity, see Fig. S4), with a clear contribution of FE emission. The PL spectrum peak anyway coincides with the FE emission (see Fig. 3b) that, even if overall less intense, is much narrower, and thus has a higher peak intensity.

At 100 K, the higher intensity in the high wavelength range observed under cw-excitation is instead due to the appearance of the LT1 peak that is not visible in the nanosecond spectrum.

Below 100 K, the progressive intensity decrease of FE emission, and the corresponding increase of BE, LT1 and LT2, leads to a cw-PL peak shift from the FE peak to a value between the BE and LT1 peak wavelengths.

Finally, the ns-PL spectrum acquired at 20 K (Fig. S2c) below the ASE threshold is well reproduced by two Gaussian bands: the peak at the lower wavelength is relative to BE emission, while the second is a new one only visible below 100 K. The cw-PL spectrum, with a clearly different line-shape with respect to the nanosecond pumping emission, shows a further emission band at a high wavelength and is well reproduced by four Gaussian bands. The comparison between the peaks contributing to the cw-PL and ns-PL at 20 K allows us to conclude that the emission at 20 K under nanosecond pumping is mainly due to BE emission, with a lower contribution of LT1, without evident contributions of FE and LT2. In contrast, the cw-PL at 20 K is dominated by LT1 and LT2 peaks, with a minor contribution of BE and a very small contribution of FE.

The difference between the emitting states observed under nanosecond and cw pumping can be ascribed to the different excitation regimes in the two experiments. The cw-measurements are performed at an excitation power density of about 0.3 W $cm^{-2}$, while the nanosecond spectra are acquired at an excitation density between 1 μJ $cm^{-2}$ at 20 K and 140 μJ $cm^{-2}$ at RT, corresponding to an average power density of between 300 W $cm^{-2}$ and 47 kW $cm^{-2}$. For this reason, in the cw-measurements, a contribution of all the emitting states is observed, with a particular contribution from the ones at lower energy that can be indirectly excited by energy migration from the higher lying ones. In contrast, in nanosecond measurements, the states with low spatial density are saturated, thus not providing a visible contribution to the emission.[67]

The observed lineshape difference between the cw and nanosecond spectra at 20 K thus indirectly confirms that the LT2 emission comes from defect states with a low density, and provides evidence of a relatively high density of the states originating from the LT1 band (see the SI for further details). Considering the energy difference between the BE emission and the LT1 and LT2 emissions, that is about 28 meV and 68 meV, respectively, we can ascribe LT1 and LT2 emissions to shallow defects that, according to theoretical calculations in the literature, are mainly due to Br vacancies and MA interstitials.[73] Tentative attribution can also be found in experimental papers to bromide vacancies or lead excess due to MABr termination at the surface of $MAPbBr_3$,[45] antisite substitution of MABr,[57] or generic crystalline defects.[44]

On the other hand, the very small contribution of FE emission, even under cw pumping, demonstrates that at 20 K, the contribution of intrinsic emission is negligible.

Finally, by comparing the ASE peak wavelength and threshold temperature dependence with the cw-PL peaks temperature dependence, we can conclude that the ASE comes from BE for the following reasons:

(1) Any contribution of LT1 and LT2 to ASE can be ruled out, as the ASE band is visible throughout the entire temperature range, while these two peaks are only visible in the low temperature range. In addition, the ASE band has to be in the emission range of the involved transition, often red-shifted with respect to the corresponding PL peak. In contrast, both LT1 and LT2, when present, show a peak wavelength higher than the ASE one.

(2) The lack of discontinuity in the ASE peak shift and threshold variation with the temperature suggest that there are no abrupt variations of the states generating the ASE in the investigated temperature range.

(3) The ASE peak shift is qualitatively similar to the BE peak one, with a temperature-independent peak wavelength from RT to 200 K, followed by a first weak shift down to 100 K and a stronger one down to 20 K. In contrast, the FE peak always shows a red-shift as the temperature decreases.

(4) The FE emission intensity decreases below 100 K. If ASE is related to FE emission, a corresponding ASE threshold increase should be observed, while a strong decrease is present. In contrast, the ASE threshold variations are compatible with the corresponding BE intensity variation, with a threshold increase when the BE intensity decreases.

### ASE threshold temperature dependence

As a last step, we quantitatively investigated the ASE temperature dependence, to compare the ASE properties of the three crystalline phases, by modelling our sample as a three level laser system,[74] after having excluded any extrinsic effect related to a temperature dependence of the waveguiding properties (see the SI for further details).

The progressive PL intensity increase as the temperature decreases is the typical signature of the presence of a thermally activated non-radiative process, allowing us to write the total exciton decay rate as:

$$\frac{1}{\tau} = \frac{1}{\tau_0} + \frac{1}{\tau_{0\mathrm{nr}}} \mathrm{e}^{-\frac{E_\mathrm{a}}{kT}} \tag{1}$$

where $\tau$ is the total decay time, $\tau_0$ is the temperature-independent decay time, $\tau_{0\mathrm{nr}}$ is the coupling constant of the non-radiative process, $E_\mathrm{a}$ is the activation energy of the non-radiative process and $k$ is the Boltzmann constant.

It is then straightforward to demonstrate that the ASE threshold excitation density $D_\mathrm{th}$ can be written as (see ref. 74 for details):

$$D_\mathrm{th} = D_0 + D_1 \mathrm{e}^{-\frac{E_\mathrm{a}}{kT}} \tag{2}$$

where $D_0 = C\frac{1}{2}\left(\frac{\alpha}{\sigma} + N\right)\frac{1}{\tau_0}$ and $D_1 = C\frac{1}{2}\left(\frac{\alpha}{\sigma} + N\right)\frac{1}{\tau_{0\mathrm{nr}}}$, where $C$ is the proportionality factor between the pump rate and the excitation density, $\alpha$ is the loss coefficient, $\sigma$ is the gain cross section and $N$ is the total emitter volume density.

The best fit curves excellently reproduce the experimental data (see Fig. 2b) in the temperature ranges 20–80 K, 100–180 K and 200–300 K for the orthorhombic, tetragonal and cubic phases, respectively, for the best fit parameters presented in Table 1.

Such a good agreement confirms that the ASE threshold temperature dependence is due to the thermal activation of a non-radiative process as the temperature increases, whatever is the crystalline phase of $\mathrm{MAPbBr_3}$.

Based on the above considerations, a reasonable scheme of the energy levels as a function of the temperature is depicted in Fig. 4.

In addition, a comparison between the best fit parameters values allows us to get an interesting insight into the differences between the different phases, suggesting that the orthorhombic phase is the one with the best ASE properties.

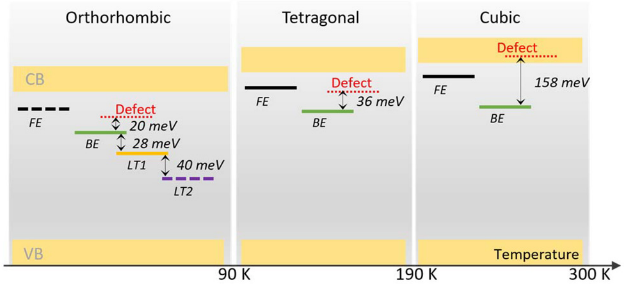

**Fig. 4** Energy level scheme as a function of the temperature (and thus the crystalline phase). The yellow stripes represent the valence band (VB) and the conduction band (CB), the dashed lines represent the levels whose emission is not visible under nanosecond pumping, while the dotted red lines correspond to the position of the non-radiative defects involved in the thermally activated ASE threshold increase.

First, the orthorhombic phase shows the lowest activation energy of the non-radiative process, followed by the tetragonal phase (with an $E_\mathrm{a}$ values about 1.8 times larger) and by the cubic phase (with an $E_\mathrm{a}$ values about 8 times larger). Such a difference shows a variation of the energy difference between the BE levels and the non-radiative defects in the three phases.

Having the lowest value of $E_\mathrm{a}$, the orthorhombic phase shows, among the three phases, a temperature-induced threshold increase at lower temperatures, but also the smallest temperature-induced increase (see Fig. S6a).

We further observe that the orthorhombic phase also shows the lowest $D_0$ (corresponding to the ASE threshold in the $T \to 0$ K limit) value of (2.390 ± 0.077) μJ $\mathrm{cm^{-2}}$, which is about 3 times lower than the tetragonal one, and about 10.5 times lower than the cubic one.

Finally, the orthorhombic phase also shows the lowest value of $D_0 + D_1$, which would correspond to the ASE threshold in the $T \to \infty$ K limit, about 1.5 times lower than the tetragonal phase, and about 1300 times lower than the cubic phase one.

For all these reasons, we can conclude that the phase intrinsically showing the best ASE properties is the orthorhombic one, followed by the tetragonal and the cubic one.

Thus, the cubic phase, which is the one showing ASE at room temperature, is characterized by the strongest ASE temperature dependence and the highest values of the ASE threshold (see the SI for further details).

In addition, the cubic phase also shows by far the largest value of $D_1/D_0$, about 2 orders of magnitudes higher than those of the other two phases. As this parameter coincides with $\tau_0/\tau_{0\mathrm{nr}}$, this difference shows a much lower $\tau_{0\mathrm{nr}}$ relative value with respect to $\tau_0$, and thus a much higher relative role of the non-radiative relaxation.

To further compare the ASE properties of the three phases, we also simulated the ASE threshold temperature

**Table 1** Best fit parameters obtained by fitting eqn (2) to the experimental values of the ASE threshold as a function of the temperature

| Temperature | $E_\mathrm{a}$ [meV] | $D_0$ [μJ $\mathrm{cm^{-2}}$] | $D_1$ [μJ $\mathrm{cm^{-2}}$] | $D_1/D_0$ |
|---|---|---|---|---|
| 20 K ≤ $T$ ≤ 80 K | 19.7 ± 1.1 | 2.390 ± 0.077 | 99 ± 15 | 41.4 ± 6.4 |
| 100 K ≤ $T$ ≤ 180 K | 35.6 ± 6.9 | 7.3 ± 1.1 | 148 ± 60 | 20 ± 9 |
| 200 K ≤ $T$ ≤ 300 K | 158 ± 12 | 25.1 ± 6.2 | (1.30 ± 0.6)$10^5$ | (5.1 ± 2.7) $10^3$ |

dependence for all the phases over the whole temperature range by keeping all the parameters fixed to the best fit ones (see Fig. S6b). These curves thus simulate the ASE threshold temperature dependence of an ideal $MAPbBr_3$ film, with a single-crystalline phase and no phase transitions. The obtained curves allow us to observe that the phase with the lowest ASE threshold would be the orthorhombic one between 20 K and 80 K, the tetragonal one between 80 K and about 370 K, and the orthorhombic again above 370 K. In contrast, the cubic phase is never the phase with the lowest ASE threshold.

## Conclusions

In this work, we investigated the temperature dependence of the spontaneous emission and ASE properties of a solution-processed $MAPbBr_3$ thin film in the 20–300 K range.

We demonstrate that the ASE threshold is strongly temperature dependent, due to the thermal activation of non-radiative processes. In addition, the ASE temperature dependence shows clear discontinuities at around 90 K and 190 K, related to the orthorhombic–tetragonal and tetragonal–cubic phase transitions, respectively, affecting both the activation energies and the coupling rates of the non-radiative process.

We also show that the film emission exhibits the interplay of emission of Free Excitons (FEs), Bound Excitons (BEs), and trap states (visible only below 100 K), with relative contributions depending not only on the temperature, but also on the excitation regimes with differences between spectra under continuous wave and nanosecond pumping.

Finally, we show that the ASE comes from BE in the whole temperature range and that, among the three phases, the orthorhombic one shows the intrinsically best ASE properties, with the lowest ASE values and the smallest temperature dependence.

Our results, beyond providing a detailed understanding of the basic optical properties of $MAPbBr_3$ thin films, evidence a strong dependence of the intrinsic ASE properties on the crystalline phase, suggesting that proper control of the crystalline phase showing a gain at room temperature can provide a powerful way to optimize the ASE and lasing properties of hybrid lead halide perovskites.

## Author contributions

Conceptualization: M. L. D. G., M. A., A. B. and C. S.; methodology: M. L. D. G. and M. A.; investigation: M. L. D. G., T. L. and M. A.; formal analysis: M. L. D. G., T. L. and M. A.; resources: A. B., C. S. and N. F. J.; funding acquisition: M. A. and C. S.; writing – original draft preparation: M. L. D. G. and M. A.; writing – review and editing: A. B., C. S., N. F. J. and T. L.; supervision: M. A. M. L. D. G. and M. A. have equally contributed. All authors have read and agreed to the published version of the manuscript.

## Conflicts of interest

The authors declare no conflicts of interest.

## Data availability

The data supporting this article have been included as part of the supplementary information (SI). Supplementary information is available. See DOI: https://doi.org/10.1039/d5nr04524j.

## Acknowledgements

The authors acknowledge support from the Singapore Ministry of Education MOE Tier 2 (Grant No. MOE-T2EP50222-0015).

This work was partially funded by the Italian Ministry of University (MUR) under Contract P2022B3W29 (PRIN – PNRR 2022 – LOGIFIB), within the EU – Next Generation EU programme, Mission 4, Component 1, CUP: B53D23028440001.

## References

1 H. Zhu, L. Pan, F. T. Eickemeyer, M. A. Hope, O. Ouellette, A. Q. M. Alanazi, J. Gao, T. P. Baumeler, X. Li, S. Wang, S. M. Zakeeruddin, Y. Liu, L. Emsley and M. Grätzel, *ACS Energy Lett.*, 2022, **7**, 1112.
2 T. M. Koh, H. Wang, Y. F. Ng, A. Bruno, S. Mhaisalkar and N. Mathews, *Adv. Mater.*, 2022, **34**, 2104661.
3 H. J. Snaith, *Nat. Mater.*, 2018, **17**, 372.
4 S. D. Stranks and H. J. Snaith, *Nat. Nanotechnol.*, 2015, **10**, 391.
5 M. B. Johnston and L. M. Herz, *Acc. Chem. Res.*, 2016, **49**, 146.
6 T. M. Brenner, D. A. Egger, L. Kronik, G. Hodes and D. Cahen, *Nat. Rev. Mater.*, 2016, **1**, 15007.
7 M. Gratzel, *Nat. Mater.*, 2014, **13**, 838.
8 M. A. Green, A. Ho-Baillie and H. J. Snaith, *Nat. Photonics*, 2014, **8**, 506.
9 N. G. Park, *J. Phys. Chem. Lett.*, 2013, **4**, 2423.
10 H. Zhou, Q. Chen, G. Li, S. Luo, T. Song, H.-S. Duan, Z. Hong, J. You, Y. Liu and Y. Yang, *Science*, 2014, **345**, 542.
11 W. Nie, H. Tsai, R. Asadpour, J.-C. Blancon, A. J. Neukirch, G. Gupta, J. J. Crochet, M. Chhowalla, S. Tretiak, M. A. Alam, H.-L. Wang and A. D. Mohite, *Science*, 2015, **347**, 522.
12 Q. Dong, Y. Fang, Y. Shao, P. Mulligan, J. Qiu, L. Cao and J. Huang, *Science*, 2015, **347**, 967.
13 L. M. Herz, *ACS Energy Lett.*, 2017, **2**, 1539.
14 N. K. Kumawat, X.-K. Liu, D. Kabra and F. Gao, *Nanoscale*, 2019, **11**, 2109.
15 S. D. Stranks, V. M. Burlakov, T. Leijtens, J. M. Ball, A. Goriely and H. J. Snaith, *Phys. Rev. Appl.*, 2014, **2**, 034007.

16 H. Cho, S. H. Jeong, M. H. Park, Y. H. Kim, C. Wolf, C. L. Lee, J. H. Heo, A. Sadhanala, N. S. Myoung, S. Yoo, S. H. Im, R. H. Friend and T. W. Lee, *Science*, 2015, **350**, 1222.

17 K. Lin, J. Xin, L. N. Quan, F. P. G. de Arquer, X. Gong, J. Lu, L. Xie, W. Zhao, D. Zhang, C. Yan, W. Li, X. Liu, Y. Lu, J. Kirman, E. H. Sargent, Q. Xiong and Z. Wei, *Nature*, 2018, **562**, 245.

18 Y. Cao, N. Wang, H. Tian, J. Guo, Y. Wei, H. Chen, Y. Miao, W. Zou, K. Pan, Y. He, H. Cao, Y. Ke, M. Xu, Y. Wang, M. Yang, K. Du, Z. Fu, D. Kong, D. Dai, Y. Jin, G. Li, H. Li, Q. Peng, J. Wang and W. Huang, *Nature*, 2018, **562**, 249.

19 Q. Van Le, H. W. Jang and S. Y. Kim, *Small Methods*, 2018, **2**, 1700419.

20 S. A. Veldhuis, P. P. Boix, N. Yantara, M. Li, T. C. Sum, N. Mathews and S. G. Mhaisalkar, *Adv. Mater.*, 2016, **28**, 6804.

21 B. R. Sutherland and E. H. Sargent, *Nat. Photonics*, 2016, **10**, 295.

22 X. Y. Chin, D. Cortecchia, J. Yin, A. Bruno and C. Soci, *Nat. Commun.*, 2015, **6**, 7383.

23 M. L. De Giorgi and M. Anni, *Appl. Sci.*, 2019, **9**, 21.

24 X. Cao, S. Xing, R. Lai, Y. Lian, Y. Wang, J. Xu, C. Zou, B. Zhao and D. Di, *Adv. Funct. Mater.*, 2023, **33**, 2211841.

25 Z. Zhan, Z. Liu, J. Du, S. Huang, Q. Li, Z. Hu, J. Luo, Y. Yang, S. Dong, L. Wang, J. Tang and Y. Leng, *ACS Photonics*, 2023, **10**, 3077.

26 J. Li, J. Si, L. Gan, Y. Liu, Z. Ye and H. He, *ACS Appl. Mater. Interfaces*, 2016, **8**, 32978.

27 A. O. Murzin, B. V. Stroganov, C. Günnemann, S. B. Hammouda, A. V. Shurukhina, M. S. Lozhkin, A. V. Emeline and Y. V. Kapitonov, *Adv. Opt. Mater.*, 2020, **8**, 2000690.

28 Z. Zhang, H. Wang, Y. Zhang, K. Li, X. Zhan, B. Gao, Q. Chen and H. Sun, *Phys. Chem. Chem. Phys.*, 2017, **19**, 2217.

29 Y. Zhang, B. Zhang, Y. Fu, F. Dou, J. Guo and X. Zhang, *Mater. Today Phys.*, 2022, **24**, 100686.

30 P. Liu, C. Gu and Q. Liao, *ACS Omega*, 2021, **6**, 34021.

31 Z. Wang, M. Luo, Y. Liu, M. Li, M. Pi, J. Yang, Y. Chen, Z. Zhang, J. Du, D. Zhang, Z. Liu and S. Chen, *Small*, 2021, **17**, 2101107.

32 S. A. Veldhuis, Y. K. E. Tay, A. Bruno, S. S. H. Dintakurti, S. Bhaumik, S. K. Muduli, M. Li, N. Mathews, T. C. Sum and S. G. Mhaisalkar, *Nano Lett.*, 2017, **17**, 7424.

33 J. R. Harwell, G. L. Whitworth, G. A. Turnbull and I. D. W. Samuel, *Sci. Rep.*, 2017, **7**, 11727.

34 M. L. De Giorgi, T. Lippolis, N. F. Jamaludin, C. Soci, A. Bruno and M. Anni, *J. Phys. Chem. C*, 2020, **124**, 10696.

35 E. Lafalce, C. Zhang, Y. Zhai, D. Sun and Z. V. Vardeny, *J. Appl. Phys.*, 2016, **120**, 143101.

36 Z. Wang, M. Luo, Y. Liu, M. Li, M. Pi, J. Yang, Y. Chen, Z. Zhang, J. Du, D. Zhang, Z. Liu and S. Chen, *Small*, 2021, **17**, 2101107.

37 H.-H. Fang, R. Raissa, M. Abdu-Aguye, S. Adjokatse, G. R. Blake, J. Even and M. A. Loi, *Adv. Funct. Mater.*, 2015, **25**, 2378.

38 A. E. J. Hoffman, R. A. Saha, S. Borgmans, P. Puech, T. Braeckevelt, M. B. J. Roeffaers, J. A. Steele, J. Hofkens and V. Van Speybroeck, *APL Mater.*, 2023, **11**, 041124.

39 C. C. Stoumpos, C. D. Malliakas and M. G. Kanatzidis, *Inorg. Chem.*, 2013, **52**, 9019.

40 M. R. Filip, G. E. Eperon, H. J. Snaith and F. Giustino, *Nat. Commun.*, 2014, **5**, 5757.

41 A. Osherov, E. M. Hutter, K. Galkowski, R. Brenes, D. K. Maude, R. J. Nicholas, P. Plochocka, V. Bulović, T. J. Savenije and S. D. Stranks, *Adv. Mater.*, 2016, **28**, 10757.

42 M. Keshavarz, M. Ottesen, S. Wiedmann, M. Wharmby, R. Küchler, H. Yuan, E. Debroye, J. A. Steele, J. Martens, N. E. Hussey, M. Bremholm, M. B. J. Roeffaers and J. Hofkens, *Adv. Mater.*, 2019, **31**, 1900521.

43 Y. Liu, H. Lu, J. Niu, H. Zhang, S. Lou, C. Gao, Y. Zhan, X. Zhang, Q. Jin and L. Zheng, *AIP Adv.*, 2018, **8**, 095108.

44 D. Priante, I. Dursun, M. S. Alias, D. Shi, V. A. Melnikov, T. K. Ng, O. F. Mohammed, O. M. Bakr and B. S. Ooi, *Appl. Phys. Lett.*, 2015, **106**, 081902.

45 D. Guo, D. Bartesaghi, H. Wei, E. M. Hutter, J. Huang and T. J. Savenije, *J. Phys. Chem. Lett.*, 2017, **8**, 4258.

46 H. S. Bawazir, S. M. H. Qaid, H. M. Ghaithan, K. K. AlHarbi, A. F. Bin Ajaj and A. S. Aldwayyan, *Photonics*, 2023, **10**, 21.

47 H. C. Woo, J. W. Choi, J. Shin, S.-H. Chin, M. H. Ann and C.-L. Lee, *J. Phys. Chem. Lett.*, 2018, **9**, 4066.

48 F. Ruf, M. F. Aygüler, N. Giesbrecht, B. Rendenbach, A. Magin, P. Docampo, H. Kalt and M. Hetterich, *APL Mater.*, 2019, **7**, 031113.

49 T. S. Kao, Y.-H. Chou, C.-H. Chou, F.-C. Chen and T.-C. Lu, *Appl. Phys. Lett.*, 2014, **105**, 231108.

50 L. Qin, L. Lv, C. Li, L. Zhu, Q. Cui, Y. Hu, Z. Lou, F. Teng and Y. Hou, *RSC Adv.*, 2017, **7**, 15911.

51 M. L. De Giorgi, A. Perulli, N. Yantara, P. P. Boix and M. Anni, *J. Phys. Chem. C*, 2017, **121**, 14772.

52 A. Balena, A. Perulli, M. Fernandez, M. L. De Giorgi, G. Nedelcu, M. V. Kovalenko and M. Anni, *J. Phys. Chem. C*, 2018, **122**, 5813.

53 A. Cretí, M. Lomascolo, Y. Zhang, M. L. De Giorgi, O. F. Mohammed and M. Anni, *Adv. Opt. Mater.*, 2023, **11**, 2202062.

54 C. Triolo, M. L. De Giorgi, A. Lorusso, A. Cretì, S. Santangelo, M. Lomascolo, M. Anni, M. Mazzeo and S. Patané, *Nanomaterials*, 2022, **12**, 211.

55 H. He, Q. Yu, H. Li, J. Li, J. Si, Y. Jin, N. Wang, J. Wang, J. He, X. Wang, Y. Zhang and Z. Ye, *Nat. Commun.*, 2016, **7**, 10896.

56 S. Milanese, M. L. De Giorgi, L. Cerdán, M.-G. La-Placa, N. F. Jamaludin, A. Bruno, H. J. Bolink, M. V. Kovalenko and M. Anni, *Molecules*, 2022, **27**, 4261.

57 C. Chen, X. Hu, W. Lu, S. Chang, L. Shi, L. Li, H. Zhong and J. Han, *J. Phys. D:Appl. Phys.*, 2018, **51**, 45105.

58 E. Ghavidel, A. Di Carlo, A. Ishteev, J. Barichello, K. Konstantinova, D. Saranin, V. Campanari, F. Martelli, B. Paci, A. Generosi, M. Guaragno, A. Cricenti, D. Becerrill, M. Luce, F. Matteocci and A. Di Trolio, *J. Mater. Chem. C*, 2024, **12**, 13141.

59 K.-H. Wang, L.-C. Li, M. Shellaiah and K. W. Sun, *Sci. Rep.*, 2017, **7**, 13643.

60 M. I. Dar, G. Jacopin, S. Meloni, A. Mattoni, N. Arora, A. Boziki, S. M. Zakeeruddin, U. Rothlisberger and M. Grätzel, *Sci. Adv.*, 2016, **2**, e1601156.

61 C. Wolf, J.-S. Kim and T.-W. Lee, *ACS Appl. Mater. Interfaces*, 2017, **9**, 10344.

62 J. Shi, H. Zhang, Y. Li, J. J. Jasieniak, Y. Li, H. Wu, Y. Luo, D. Liab and Q. Meng, *Energy Environ. Sci.*, 2018, **11**, 1460.

63 F. Chen, C. Zhu, C. Xu, P. Fan, F. Qin, A. G. Manohari, J. Lu, Z. Shi, Q. Xu and A. Pan, *J. Mater. Chem. C*, 2017, **5**, 7739.

64 J. Dai, H. G. Zheng, C. Zhu, J. F. Lu and C. X. Xu, *J. Mater. Chem. C*, 2016, **4**, 4408.

65 H. Yu, W. Wu, Q. Wang, J. Liu, D. Kong and Y. Gao, *Mater. Today Phys.*, 2022, **22**, 100621.

66 J. Hu, Y. Zhang and X. Zhang, *J. Phys. Chem. Lett.*, 2022, **13**, 6093.

67 C. Wehrenfennig, M. Liu, H. J. Snaith, M. B. Johnston and L. M. Herz, *APL Mater.*, 2014, **2**, 081513.

68 T. Baikie, Y. Fang, J. M. Kadro, M. Schreyer, F. Wei, S. G. Mhaisalkar, M. Graetzel and T. J. White, *J. Mater. Chem. A*, 2013, **1**, 5628.

69 K. Wu, A. Bera, C. Ma, Y. Du, Y. Yang, L. Li and T. Wu, *Phys. Chem. Chem. Phys.*, 2014, **16**, 22476.

70 W. Kong, Z. Ye, Z. Qi, B. Zhang, M. Wang, A. Rahimi-Iman and H. Wu, *Phys. Chem. Chem. Phys.*, 2015, **17**, 16405.

71 F. Panzer, S. Baderschneider, T. P. Gujar, T. Unger, S. Bagnich, M. Jakoby, H. Bässler, S. Hüttner, J. Köhler, R. Moos, M. Thelakkat, R. Hildner and A. Köhler, *Adv. Opt. Mater.*, 2016, **4**, 917.

72 G. Xing, N. Mathews, S. S. Lim, N. Yantara, X. Liu, D. Sabba, M. Grätzel, S. Mhaisalkar and T. C. Sum, *Nat. Mater.*, 2014, **13**, 476.

73 S. G. Motti, D. Meggiolaro, S. Martani, R. Sorrentino, A. J. Barker, F. De Angelis and A. Petrozza, *Adv. Mater.*, 2019, **31**, 1901183.

74 G. Morello, S. Milanese, M. L. De Giorgi, N. Calisi, S. Caporali, F. Biccari, N. Falsini, A. Vinattieri and M. Anni, *Nanomaterials*, 2023, **13**, 306.